

On the application of an optimized Frequency-Phase Modulated waveform for enhanced infrared thermal wave radar imaging of composites

Saeid Hedayatrasa^{1,2*}, Gaétan Poelman^{1,2}, Joost Segers¹, Wim Van Paepegem¹
and Mathias Kersemans^{1*}

¹ Mechanics of Materials and Structures (UGent-MMS), Department of Materials, Textiles and Chemical Engineering, Ghent University, Technologiepark-Zwijnaarde 46, 9052 Zwijnaarde, Belgium

²SIM Program M3 DETECT-IV, Technologiepark-Zwijnaarde 48, B-9052 Zwijnaarde, Belgium

Abstract

Thermal Wave Radar (TWR) imaging employs the concept of pulse compression in order to obtain an increased probing depth and depth resolution in infrared thermographic testing of materials. The efficiency of the TWR imaging is highly dependent on the nature of the employed excitation signal. Most studies exploit the use of an excitation signal with an analogue frequency modulation (e.g. sweep signal) or a discrete phase modulation (e.g. Barker coded signal). Recently, a novel frequency-phase modulated (FPM) waveform was introduced, and computationally verified by the current authors, which couples the concept of frequency- and phase modulation to each other in view of obtaining an optimized excitation signal for improved TWR imaging.

This paper experimentally investigates the performance of the novel optimized FPM waveform for the inspection of glass and carbon fiber reinforced polymer (GFRP and CFRP) composites, using an optical infrared thermography set-up in reflection mode. The response of the halogen lamps to the FPM waveform is measured, and further the influence of the electro-thermal latency of excitation lamps on the applicability of the novel FPM excitation signal is analytically investigated. Then, the performance of the FPM waveform is experimentally investigated for both glass- and carbon fiber reinforced polymers with defects of different depths and sizes. A comparative analysis is performed with amplitude modulated (classical lock-in), frequency modulated (sweep) and phase modulated (Barker coded) excitation, each with the same time duration as the FPM waveform. The novel FPM waveform outperforms these existing waveforms in terms of defect detectability and contrast-to-noise ratio, especially for the deeper defects. Different central frequencies are examined and the improved performance of the FPM waveform in TWR imaging is demonstrated in all cases.

Keywords: Infrared Thermography; Frequency-Phase Modulation (FPM); Electro-Thermal Latency; Pulse Compression; Composite; Thermal Wave Radar

1. Introduction

Optical infrared thermography is a contact-free non-destructive testing (NDT) technique which has been widely used for fast full-field inspection of large composite components made from

* Corresponding Authors:

saeid.hedayatrasa@ugent.be (S. Hedayatrasa), mathias.kersemans@ugent.be (M. Kersemans).

glass and carbon fiber reinforced polymer (GFRP and CFRP) [1, 2]. The technique requires a set of optical (flash, halogen or LED) lamps to illuminate the sample and to induce heat waves at the surface. The heat diffuses through the sample and any thermal diffusivity mismatch (introduced by defects' interfaces) alters the heat diffusion process. This leads to local variations of the temperature evolution at the inspection surface, which can be detected and quantified by proper post-processing of the recorded thermal images (e.g. [3-10]). The excitation may be a short broadband pulse (i.e. flash thermography [11]), a long pulse (i.e. step-heating [12] or long-pulse [13] thermography), a sinusoidal waveform (i.e. lock-in thermography) [14], or a frequency and/or phase modulated waveform [6, 15-21].

Thermal wave radar (TWR) is an efficient thermographic technique which uses modulated excitation waveforms in combination with pulse compression in order to obtain increased signal-to-noise ratio (SNR), depth resolution and probing depth of infrared thermography. In fact the application of the pulse compression provides an estimate of the impulse response of the sample as close as possible to the one obtainable by a pulsed-excitation (Dirac delta-like stimulus), but with a higher SNR. TWR was initially implemented for optical infrared thermography using frequency modulated (sweep) excitation waveforms [6, 18, 19], and not much later, binary phase modulated (Barker coded) waveforms were used [20, 22-24]. The technique has later on been applied to eddy current thermography [7, 25, 26].

Various research works have investigated the impact of frequency sweep parameters [27] or the length of the Barker coded waveform [23] on the depth resolvability of TWR. In terms of performance, the Barker coded waveform has shown to be superior to the sweep excitation waveform [21, 24, 28]. Still, the Barker codes (of various bit lengths) are designed for maximized pulse compression quality in (electromagnetic) radio wave radar application, and as such they are not necessarily the optimal choice for thermal wave radar applications. This is easily understood considering the distorted thermal response to a coded waveform due to diffusive (i.e., overly damped and dispersive) nature of heat waves. Moreover, a longer bit length (which normally leads to higher pulse compression quality) leads to a longer excitation and that is not desired in thermographic inspection in order to avoid: (i) excessive heating of the test piece, (ii) blurring effects due to lateral heat diffusion and (iii) interruption by the heat wave reflected from the backside of the sample. This is particularly essential when inspecting fiber reinforced composite laminates which dissipate heat more rapidly due to their higher in-plane thermal diffusivity (along the fibers' direction).

In this regard, a novel discrete frequency-phase modulated (FPM) waveform was recently introduced by the current authors [29] and its short 5-bit modulation code was optimized for maximized depth resolvability of TWR. In fact, the discretely modulated FPM waveform allows for both (i) broadening the excitation spectrum for increased diffusivity length (i.e. probing depth) and (ii) maximizing the pulse compression quality specifically for the (diffusive) heat wave problem. The analytical and 3D finite element (FE) results showed that the optimized FPM waveforms outperform both the frequency sweep and the Barker coded excitation when considering the same central frequency and the same excitation duration.

The discretely modulated FPM waveform is comprised of five sub-pulses with sudden amplitude variations at the modulation points, which may be easily applied in a simulation environment. However, in practice, such a waveform requires fast reaction time of the excitation system. In an optical thermographic set-up, the reaction time mainly depends on the type and thermal inertia of the optical source. Mostly, halogen lamps are used for the optical excitation and it was already proposed to take the latency of the optical source explicitly into account [30]. LED lamps are an alternative optical source, and due to their short response time they have been used for discrete modulation of the excitation waveform [22] .

This paper is dedicated to the experimental validation of the FPM waveform for TWR imaging of composite laminates. First, the influence of the latency of the excitation lamps is studied, and its impact on the performance of the novel FPM waveform is discussed. Then, the enhanced performance of the optimized FPM waveform is validated for the inspection of a GFRP and a CFRP test coupon including multiple artificial defects (flat bottom holes) with various depths and sizes. The performance of the optimized FPM waveform is compared to amplitude- (lock-in), frequency- (sweep) and discrete phase- (Barker coded) modulated excitation waveforms, all with the same duration. Different central frequencies are examined and the increased probing depth and depth resolution of the optimized FPM waveform are confirmed.

The layout of the paper is as follows. In section 2, the theory of thermal wave radar is provided and the evaluated waveforms are introduced. In section 3, the experimental set-up and the test coupons are described. In section 4 the sensitivity of TWR to the latency of the excitation system is analyzed, and in section 5 the performance of the FPM waveform for the inspection of the composite test coupons is experimentally studied.

2. Thermal wave radar (TWR) and excitation waveforms

2.1. Theoretical formulation

TWR is implemented by cross-correlation of the measured thermal response $\tilde{T}(t)$ with the corresponding excitation (reference) waveform $\tilde{S}(t)$ as follows [19, 28]:

$$\chi(\tau) = \tilde{T} \otimes \tilde{S}(\tau) = \int_{-\infty}^{+\infty} \tilde{T}(t) \tilde{S}(t + \tau) dt \quad (1)$$

where \otimes denotes cross-correlation and (\sim) denotes the AC component of the signal due to the mono-polar nature of the optical excitation. In practice, this AC component is obtained by removing the DC component as a low-order polynomial interpolant of the thermal response as explained in section 5.

For computational efficiency, the cross-correlation is preferably performed in the frequency-domain [19, 31]. The output $\chi(\tau)$ of this operation is a sinc-like function which compresses the energy of the whole signal under its main lobe. The peak value $Peak_{\chi}$ and corresponding time delay lag_{χ} of the cross-correlation are then derived as:

$$Peak_{\chi} = \text{Max}(\chi(\tau)) \quad (2)$$

$$lag_{\chi} = \tau|_{\chi(\tau)=\text{Max}(\chi(\tau))} \quad (3)$$

The time delay lag_χ is an emissivity-normalized quantity which is related to the defect's depth [19]. Subsequently, the phase of cross-correlation φ_χ can be found as another emissivity-normalized quantity:

$$\varphi_\chi = \tan^{-1} \left(\frac{\chi(\tau)}{\chi_H(\tau)} \right) \bigg|_{\tau=0} \quad (4)$$

where χ_H is the cross-correlation with the Hilbert transform of $\tilde{S}(t)$ [20]. In the case of mono-frequency harmonic excitation, the phase of cross-correlation φ_χ reduces to the well-known phase of lock-in thermography.

2.2. Frequency-phase modulated (FPM) and the conventional waveforms

A comparative analysis is performed with amplitude modulated (classical lock-in), frequency modulated (sweep) and phase modulated (Barker coded) excitation waveforms, each with the same time duration as the FPM waveform (see Figure 1).

The 5-bit FPM waveform is formulated by 5 evenly spaced sub-pulses of different frequencies and phases [29]. It is defined through the following set of equations:

$$\tilde{S}_{\text{FPM}}(t) = \sum_{j=1}^5 P_j(t) \cos \left(2\pi (f_1 + (f_2 - f_1)C_{fj})t + \frac{\pi}{2} C_{\varphi j} \right) \quad (5)$$

$$P_j(t) = \begin{cases} 1 & ; \quad (j-1)/f_c \leq t < j/f_c \\ 0 & ; \quad \text{else} \end{cases} \quad (6)$$

$$[f_1, f_2] = [f_c(1+r), f_c(1-r)]; \quad r = 0.33 \quad (7)$$

$$\mathbf{C}_f = [1.00 \quad 0.75 \quad 0.5 \quad 0.25 \quad 0.00] \quad (8)$$

$$\mathbf{C}_\varphi = [C_{\varphi 1}, C_{\varphi 2}, C_{\varphi 3}, C_{\varphi 4}, C_{\varphi 5}]; \quad -1 \leq C_{\varphi j} \leq 1 \quad (9)$$

The FPM waveform has a central frequency f_c and a frequency range $[f_1, f_2]$. The frequency modulation code \mathbf{C}_f (Eq. 8) has a constant definition such that it prescribes an evenly stepped modulation frequency from the upper band limit $f_c(1+0.33)$ to the lower band limit $f_c(1-0.33)$ over the length of 5 bits. The phase modulation code \mathbf{C}_φ (Eq. 9) has a variable definition which provides flexibility to tailor the performance of the FPM waveform in view of increased depth resolvability in TWR imaging.

In a recent study by the current authors, this phase modulation code \mathbf{C}_φ was optimized (through a random brute force approach) for maximized depth resolvability in TWR imaging. Figure 1(f) shows the optimized waveform FPM. The phase codes $C_{\varphi j}$ are given on top of the individual sub-pulses. For further details on the optimized FPM signal, the reader is referred to reference [29].

For benchmarking and evaluating the performance of the FPM waveform, other conventional waveforms are also studied which all have the same time duration as the FPM waveform:

- (i) Sinusoidal (lock-in) waveforms with 10 cycles i.e. twice the central frequency (Figure 1(a)), with 5 cycles i.e. the same central frequency (Figure 1(b)), and with a single cycle i.e. the lowest frequency possible over the 5-bit duration of the FPM waveform (Figure 1(c)).
- (ii) Frequency sweep waveforms at the same central frequency and the same start and end frequency of the FPM waveform (Figure 1(d)),
- (iii) 5-bit Barker coded waveform at the same central frequency of the FPM waveform (Figure 1(e))

As shown in Figure 1(d), two frequency sweeps with linear and logarithmic (i.e. exponential) sweep rates are evaluated as defined by the following equations:

$$\tilde{S}_{\text{Sweep}}(t) = \cos(\varphi(t)) \quad (10)$$

$$\varphi(t) = \begin{cases} 2\pi \left(f_1 t + \left(\frac{f_2 - f_1}{2T} \right) t^2 \right) + \varphi_0, & \text{Linear sweep} \\ 2\pi \left(\frac{T}{\ln \left(\frac{f_2}{f_1} \right)} \left(f_1 \left(\frac{f_2}{f_1} \right)^{\frac{t}{T}} - f_1 \right) \right) + \varphi_0, & \text{Logarithmic sweep} \end{cases} \quad (11)$$

where $T = 5/f_c$ is the sweep duration and $\varphi_0 = -\pi/2$ is the initial phase. According to Equation 11, the instantaneous frequency (i.e. $f(t) = d\varphi(t)/dt$) proportionally varies with time in the linear sweep, and it exponentially varies in the logarithmic sweep. This leads to an increased power spectrum at the low frequency regime of the logarithmic sweep and, therefore, an increased probing depth.

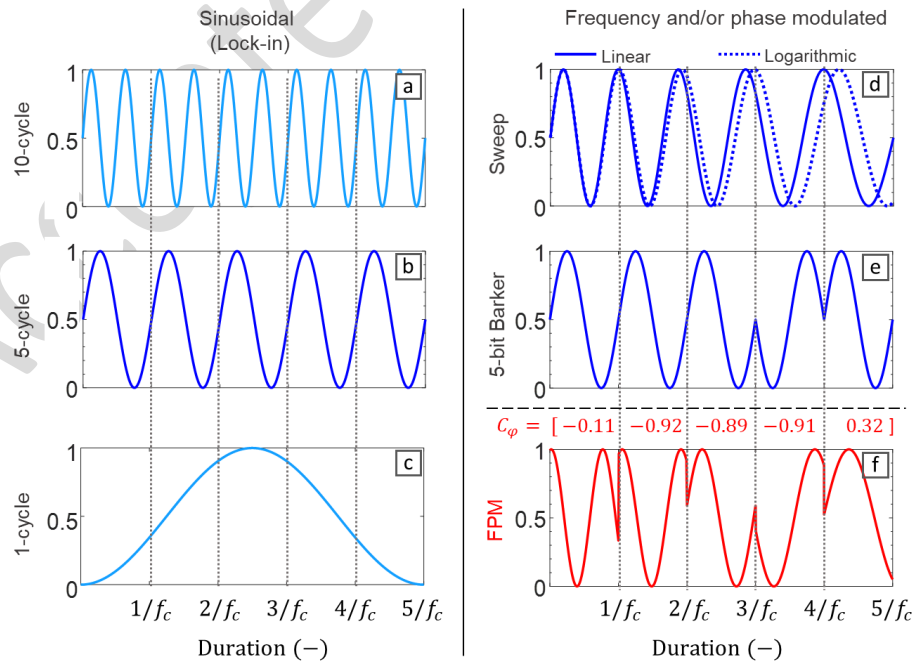


Figure 1: (a-e) The conventional waveforms and (f) the optimized FPM waveform, all with the same duration of $5/f_c$

3. Experimental set-up

3.1. Materials

A glass/polyamide-6 (TC910 Nylon6 by TenCate Cetex®) test coupon with cross-ply lay up $[(0/90)_5]_s$ and thickness 5 mm, and a carbon/epoxy test coupon with quasi-isotropic lay up $[(-45/0/45/90)_3]_s$ and thickness 5.5 mm are tested (see Figure 2). Note that the GFRP coupon is produced by black-colored polyamide-6.

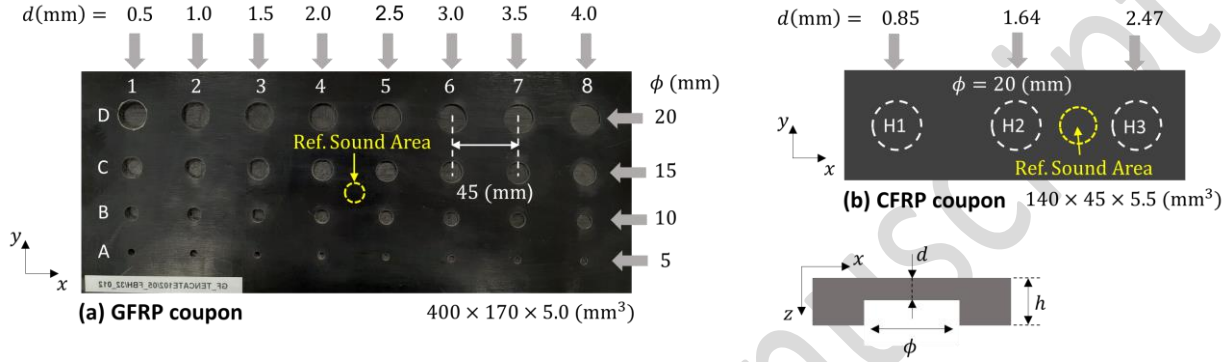


Figure 2: (a) GFRP and (b) CFRP test coupons including FBHs of different diameters and depths as artificial defects

The GFRP test coupon contains 32 flat bottom holes (FBHs) as artificial defects (see Figure 2(a)). FBHs are positioned in 4 rows with different diameters (5 to 20 mm) and in 8 columns with various depths (0.5 mm to 4 mm), including a wide range of diameter-to-depth ratio ϕ/d from 1.25 (i.e. A8) up to 40 (i.e. D1). The CFRP test coupon includes a single row of FBHs of diameter 20 mm and different depths 0.85, 1.64 and 2.47 mm (see Figure 2(b)). A reference sound area as indicated on the samples is considered for the calculation of contrast quantities and contrast-to-noise ratio (CNR). The test coupons are tested with different excitation waveforms (see further in Figure 1) at three different central frequencies 0.1, 0.05 and 0.025 Hz.

3.2. Hardware

All experiments are performed with a synchronized thermographic system (edevis® GmbH). The top side of the test coupon is illuminated using two Hedler H25s halogen lamps at a stand-off distance of around 1000 mm as schematically shown in Figure 3. Each lamp has a nominal power of 2.0 kW and a color temperature of 3200 K, and is covered with two PMMA plates which filter out the interfering infrared spectrum of the excitation source. The heating amplitude is limited to 50% of the lamps' power, and the quadratic relationship of the lamps' power with the input voltage signal is taken into account. A Si PIN photodiode (Hamamatsu S1223) with high sensitivity to the spectral range 0.32-1.1 μm (visible to near infrared) is used to measure the lamp's response and the light intensity illuminated to the sample. The photodiode has a photosensitive area of 6.6 mm², a cutoff frequency of 30 MHz and a photosensitivity of 0.45 A/W at the wavelength 660 nm (i.e. within the spectrum which the Hedler lamps emit the highest intensity of visible light). The photodiode's response is measured by a 24-bit high resolution

oscilloscope (PXIe-5922) at 50 kHz and with an input impedance of 50 Ω . The light intensity illuminated to the test coupon in the current test set-up is measured equal to 0.61 mW/mm².

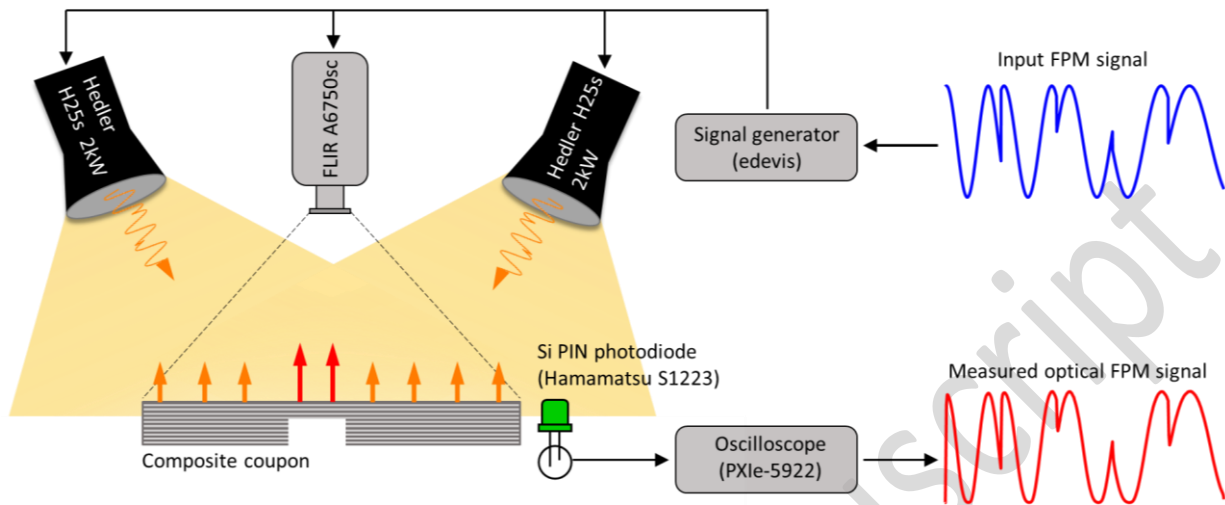


Figure 3: Schematic presentation of the optical thermographic set-up for inspection of the composite coupon in reflection mode and measurement of the lamps' response to the FPM waveform

The coupons surface temperature is measured in reflection mode (Figure 3) by a FLIR A6750sc infrared camera at a sampling rate of 10 Hz. The camera has a cryo-cooled InSb detector which operates in the spectral range of 3-5 μm and has a pixel density of 640×512 , a noise equivalent differential temperature (NEDT) of < 20 mK and a bit depth of 14 bit. In the current experimental set-up, the thermal images of test coupon have a pixel density of 1.53 pixel/mm (i.e., ~ 46 pixels over the smallest FBHs). The non-uniformity of the infrared detectors and their temporal drift are corrected through the automatic internal non-uniformity correction (NUC) system of the camera.

4. Sensitivity to electro-thermal latency of excitation system

The finite rise time of a realistic optical excitation system (e.g. Halogen lamps), combined with the discrete nature of the introduced FPM excitation signal, might degrade the performance of the FPM signal in experimenting. This section investigates the influence of the electro-thermal latency of the excitation system on the performance of the FPM signal for TWR imaging.

4.1. Measuring the latency of halogen lamps

First, the actual response of the halogen lamps in the current experimental set-up is measured using a photodiode. Photodiode is a semiconductor device which converts light energy to electric current, and its output current varies instantaneously (in $\sim \text{ns}$) and linearly by the intensity of light energy incident to its photosensitive area.

As can be seen in Figure 4(a), the photodiode of the present set-up and in the absence of any excitation has a dark current (i.e. noise level) of around $0.75 \mu\text{A}$. By application of a step excitation (i.e. turning on the lamps for 5 s at 50% power), the photodiode generates up to a maximum current of $1800 \mu\text{A}$ (Figure 4(b)) and presents the latency of the lamps in response to

the input excitation. This latency is defined by the rise time t_r of the lamp which is the time from 10% to 90% of its steady state response. A rise time of 0.305 s was obtained (see also Figure 4(b)).

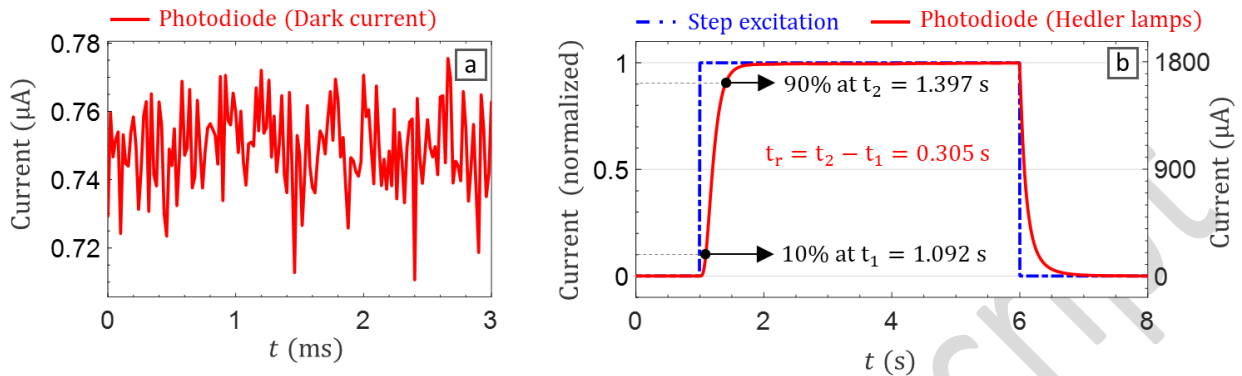


Figure 4: The output current of the photodiode (a) in dark condition and (b) by application of a step excitation to the lamps

Obviously, the measured rise time of 0.305 s is negligible compared to the excitation frequencies of interest in this study. To confirm this, the response of the lamps to the FPM waveform are further measured at the central frequencies 0.05 Hz (Figure 5(a,b)) and 0.1 Hz (Figure 5(c,d)). As expected, the lamps' response is slightly deviated from the input excitation, and its deviation is more pronounced at the modulation points (Figure 5(b,d)), particularly at the higher central frequency of 0.1 Hz (Figure 5(c,d)).

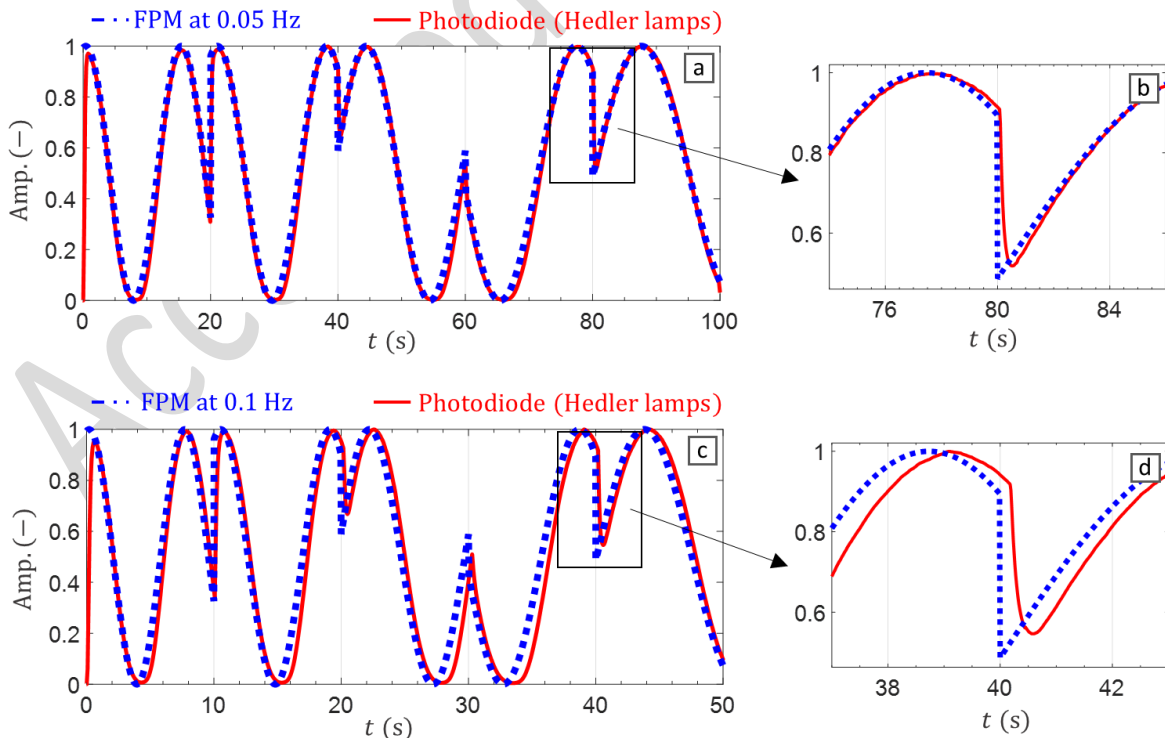


Figure 5: The lamps' response to the FPM waveform at central frequencies (a,b) 0.05 Hz and (c,d) 0.1 Hz

4.2. Simulation of electro-thermal latency

In this section, the impact of electro-thermal latency on the performance of FPM waveforms is studied and quantified by simulation. For this purpose, the latency is simulated by application of a resistor-capacitor circuit (RC-filter) as shown in Figure 6(a). Supplying a voltage S to the circuit, results in a low-pass filtered voltage S_{RC} (i.e. a latency) at the capacitor. The frequency response of the RC-filter can be derived as [32]:

$$S_{RC}(\omega) = \frac{1 - iRC\omega}{1 + (RC\omega)^2} S(\omega) \quad (12)$$

where R [Ω] is resistance of the resistor, C [F] is capacitance of the capacitor and their product RC [s] is called the time constant of the circuit. The time response of the circuit to a step excitation can be further derived as:

$$S_u(t) = \frac{1}{RC} e^{-\frac{t}{RC}} u(t) \quad (13)$$

$$u(t) = \begin{cases} 1, & t \geq 0 \\ 0, & t < 0 \end{cases} \quad (14)$$

which results in a rise time of $t_r = 2.2 RC$.

Therefore, the time constant corresponding to the measured rise time $t_r = 0.305$ s is $RC = 0.14$ s. Whereas this latency leads to a small deviation of FPM waveform at the lowest central frequency of 0.05 Hz (see Figure 5(a)), an extreme case of latency is additionally studied with a much higher time constant of $RC = 1$ s which leads to a rise time of $t_r = 2.2$ s (see Figure 6(b)). This helps with understanding the impact of latency when using lamps with higher latency, or using current lamps at a higher central frequency e.g. for inspection of thin metallic samples.

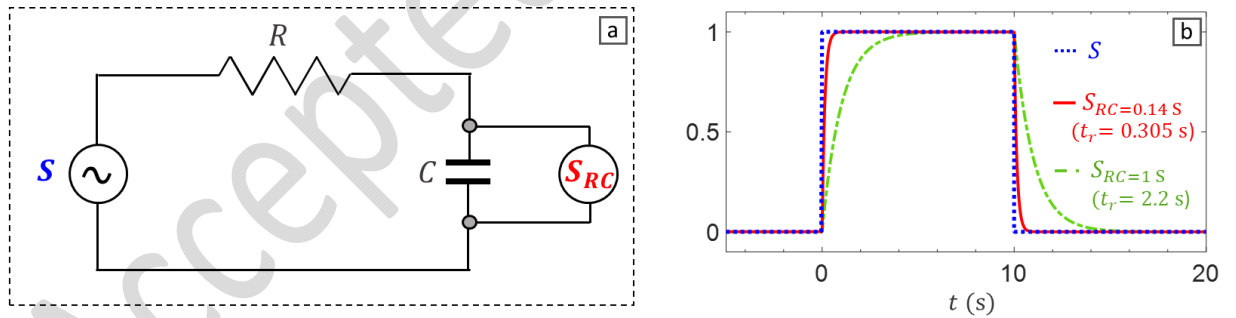


Figure 6: (a) Resistor-capacitor circuit (RC-filter) to simulate the electro-thermal latency of the excitation system, and (b) the response corresponding to the measured time constant $RC = 0.14$ s and the assumed extreme case of $RC = 1$ s

Figure 7(a) compares the AC component of original FPM waveform \tilde{S} at the central frequency 0.05 Hz, and the corresponding RC-filtered waveform \tilde{S}_{RC} . \tilde{S}_{RC} shows an initial rise time to the maximum amplitude and a delayed reaction at the modulation points, and as expected, with a significantly higher latency for the case $RC = 1$ (see the inset of Figure 7(a)). Nonetheless, comparison of the auto-correlation of both the original and the RC-filtered waveforms in Figure

7(b) indicates that even such a high latency has a minor influence on the pulse compression quality.

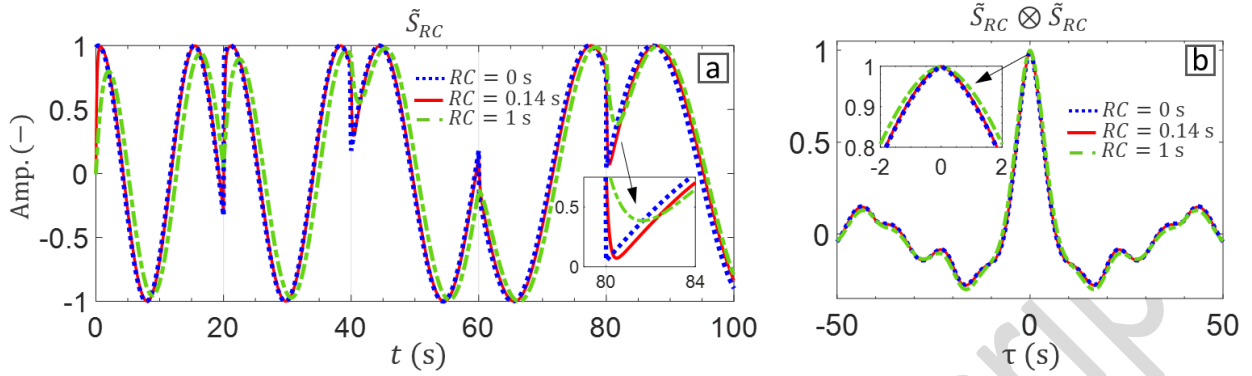


Figure 7: (a) The AC component of the optimized FPM waveform at central frequency of 0.05 Hz before and after applying the electro-thermal latency using the RC-filter and (b) the corresponding auto-correlations

4.3. Simulation of thermal wave radar (TWR)

After application of the electro-thermal latency to the FPM waveform as simulated in section 4.2, its influence on the depth resolvability of TWR for inspection of GFRP is further studied using the analytical solution of heat diffusion.

The thermal frequency response $\theta(z, \omega)$ of 1D heat diffusion through the thickness (i.e. z -axis) of a homogeneous solid with dissipation-free boundary conditions can be derived as follows [19, 21]:

$$\theta(z, \omega) = A(\omega) \exp(\beta(\omega)z) + B(\omega) \exp(-\beta(\omega)z) \quad (15)$$

$$A(\omega) = \frac{q(\omega)}{\beta(\omega)k_z} \frac{\exp(-2\beta(\omega)h)}{1 - \exp(-2\beta(\omega)h)} \quad (16)$$

$$B(\omega) = \frac{q(\omega)}{\beta(\omega)k_z} \frac{1}{1 - \exp(-2\beta(\omega)h)} \quad (17)$$

where $\omega = 2\pi f$ is the angular frequency [rad/s], h is the thickness of material [m], $q(\omega)$ is the heat flux [W/m²] applied at the inspection surface (i.e. $z = 0$), $\beta(\omega) = (1 + i)/\sqrt{2\alpha_z/\omega}$, $i = \sqrt{-1}$ and α_z is the through-the-thickness thermal diffusivity [m²/s]. For a given excitation waveform $\tilde{S}(t)$ and heating amplitude q_0 , the relevant heating load in the frequency-domain is calculated as:

$$q(\omega) = \mathcal{F}\{q_0\tilde{S}(t)\} \quad (18)$$

and the corresponding time-domain thermal response at the inspection surface is derived by:

$$\tilde{T}(t) = \mathcal{F}^{-1}\{\theta(0, \omega)\} \quad (19)$$

where \mathcal{F} and \mathcal{F}^{-1} , respectively, denote the Fourier and inverse Fourier transform operators. The surface temperature $\tilde{T}(t)$ calculated for the full thickness h corresponds to a non-defected area, while the one calculated for any smaller thickness $d < h$ corresponds to a defected area.

For calculation of the thermal response, the material properties of the GFRP test coupon are used which has a density of $\rho = 1730 \text{ kg/m}^3$, and a glass fiber volume fraction of around 43%. This results in an effective heat capacity of $C_p = 1316 \text{ J/kg.K}$ and an effective through-the-thickness thermal conductivity of $k_z = 0.45 \text{ W/m.K}$ [33].

Figure 8(a) compares the analytical thermal responses corresponding to the original FPM waveform \tilde{S} and its RC-filtered one \tilde{S}_{RC} for a 2.5 mm thick GFRP. The results clearly demonstrate the fact that the thermal response is predominantly affected by dampening effects of heat wave diffusion through-out the sample. As expected, the latency of the excitation system is particularly effective at the modulation points at which it smoothens the output excitation waveform and the resultant thermal response (see the inset of Figure 8(a)). The very sharp amplitude modulations present in \tilde{S} (in the absence of latency), induce heat waves at frequencies much higher than the central frequency and with very limited diffusion length. Therefore, the latency of the excitation becomes only important when high frequencies are of interest (e.g. for the inspection of a very shallow depth range in the material). This is further confirmed in Figure 8(b), which shows that even the excessive latency of $RC = 1$ has minor impact on the sharpness and sidelobe level of the compressed pulse.

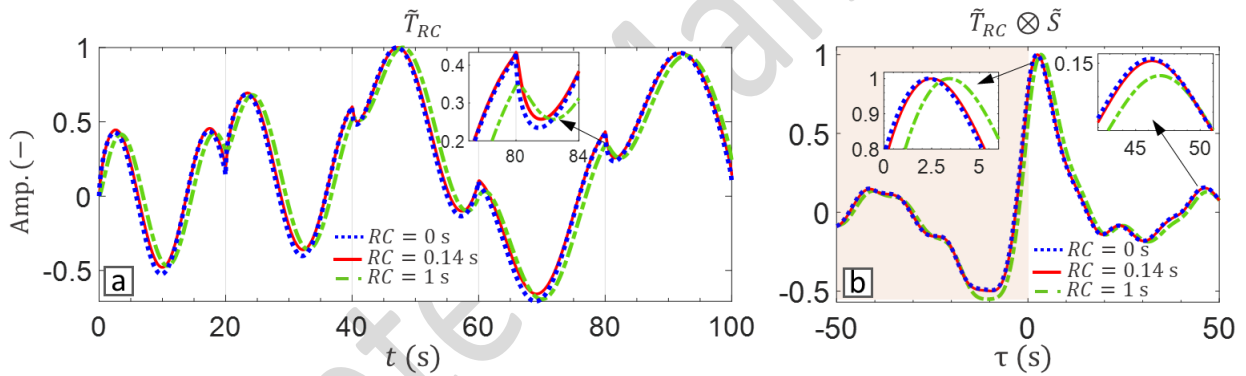


Figure 8: (a) Analytical thermal response of a 2.5 mm thick GFRP to the optimized waveform FPM at central frequency of 0.05 Hz before and after applying the electro-thermal latency (see Figure 6) and (b) the corresponding cross-correlations with the original FPM signal

Furthermore, the lag_χ and φ_χ corresponding to both the original FPM waveform \tilde{S} and its RC-filtered counterpart \tilde{S}_{RC} are calculated up to the total thickness of 5 mm for the GFRP material. The lag contrast Δlag_χ and the phase contrast $\Delta \varphi_\chi$, as compared to a sound material with a thickness of 5 mm, are then calculated (Figure 9). In order to take into account the electro-thermal latency of excitation in the calculation of cross-correlation (i.e. χ_{RC}), three different cases are assumed:

- Case A: the thermal response \tilde{T} is cross-correlated with the excitation waveform \tilde{S} . This corresponds to the theoretical situation when there is no latency in the excitation system
- Case B: the thermal response \tilde{T}_{RC} is cross-correlated with the excitation waveform \tilde{S} . This corresponds to the situation when the latency of the lamps is unknown.

- Case C: the thermal response \tilde{T}_{RC} is cross-correlated with the excitation waveform \tilde{S}_{RC} . This corresponds to the situation when the latency of the lamps is known.

Therefore the cross-correlation χ_{RC} can be defined as follows:

$$\chi_{RC} = \begin{cases} \tilde{T} \otimes \tilde{S} & , \quad \text{Case A} \\ \tilde{T}_{RC} \otimes \tilde{S} & , \quad \text{Case B} \\ \tilde{T}_{RC} \otimes \tilde{S}_{RC} & , \quad \text{Case C} \end{cases} \quad (20)$$

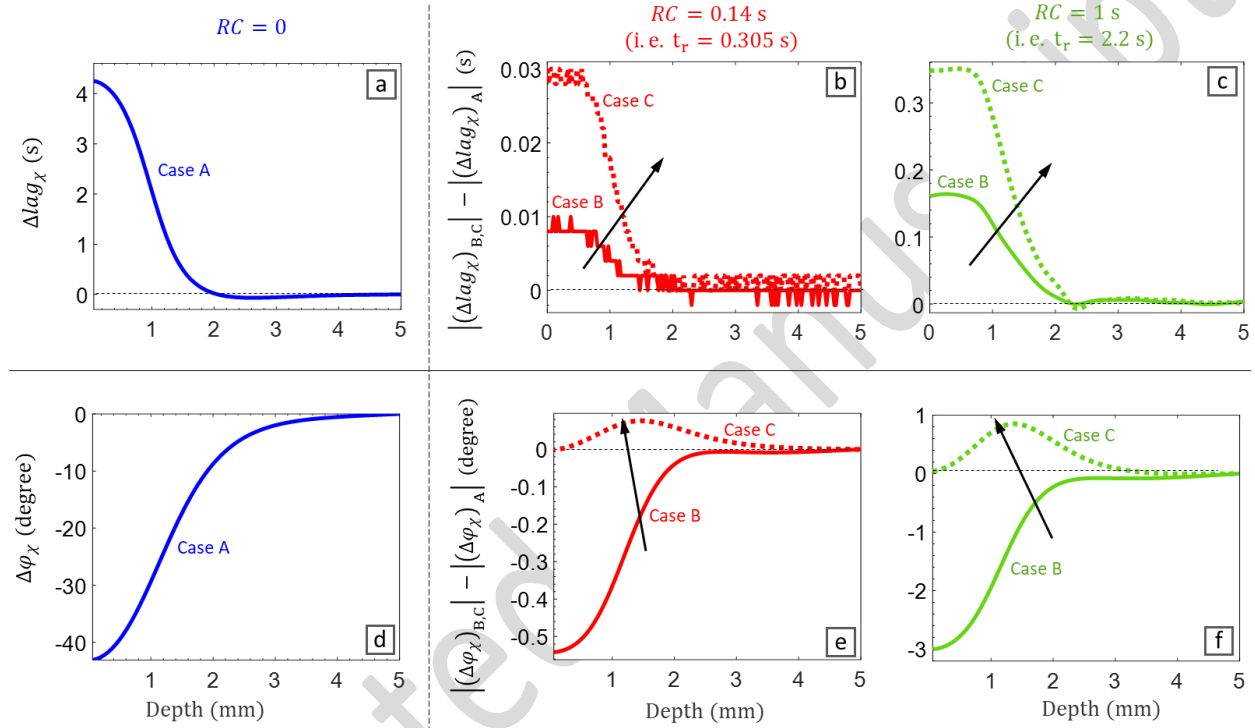


Figure 9: Depth resolvability of the optimized FPM waveform at central frequency 0.05 Hz for case A : (a) lag contrast Δlag_{χ} and (d) phase contrast $\Delta \phi_{\chi}$. Deviation of lag contrast Δlag_{χ} of cases B and C from case A: (b) $RC = 0.14$ s and (c) $RC = 1$ s. Deviation of phase contrast $\Delta \phi_{\chi}$ of cases B and C from case A: (e) $RC = 0.14$ s and (f) $RC = 1$ s

The calculated contrast quantities are compared in Figure 9. The left column of Figure 9 shows the individual contrast quantities, and the other two columns show the deviation of contrast quantities of cases B and C (i.e. with latency) from case A (i.e. without latency). The middle column corresponds to the measured time constant $RC = 0.14$ s and the right column corresponds to the assumed extreme case of latency with $RC = 1$ s.

Figure 9(a) indicates that at the central frequency of 0.05 Hz and in the absence of measurement noise, the lag contrast Δlag_{χ} can resolve a depth of up to around 2.0 mm. Furthermore, Figure 9(b,c) show that the lag contrast Δlag_{χ} slightly increases by taking into account the latency. The increased lag contrast Δlag_{χ} is particularly pronounced in case C for which a known delayed waveform is used as the reference waveform of cross-correlation. For the measured time constant $RC = 0.14$ s (Figure 9(b)), the deviation of Δlag_{χ} is so small that it

cannot be smoothly resolved by the simulation sampling frequency of 500 Hz. Overall, the results confirm that the electro-thermal latency has no negative impact on the depth resolvability of lag_{χ} .

In terms of phase contrast $\Delta\varphi_{\chi}$, Figure 9(d) shows the deeper depth resolvability of phase contrast up to around 4 mm. Moreover, Figure 9(e,f) show that the latency leads to a minor deviation of phase contrast $\Delta\varphi_{\chi}$, and that it even enhances the contrast in case C in which a known delayed waveform is used as the reference waveform of cross-correlation.

The results clearly show the negligible deviation of contrast quantities in case of $RC = 0.14$ s (Figure 9(b,e)). Even the extreme case of latency $RC = 1$ s (Figure 9(c,f)) leads to a relatively small deviation of contrast quantities.

Examination of other FPM and Barker coded waveforms indicated the same behavior with slightly different levels of sensitivity. Overall, the results suggest that a very short reaction time (e.g. using LED lamps) is not necessary at all for application of discretely coded waveforms in TWR imaging. In case very shallow depths in highly conductive media are of interest, the effects of the latency will become more important to take into account. Therefore, case A is applied in the following experimental studies, meaning that the original excitation waveform is used as the reference of cross-correlation.

5. Experimental validation of the optimized FPM waveform

5.1. GFRP sample

In this section the GFRP test coupon is inspected using the optimized FPM waveform and the conventional waveforms of the same duration (see Figure 1). First, the procedure for decoupling the AC component of thermal response is explained, and then the defect detectability of the different waveforms is compared.

5.1.1. Decoupling the AC component of thermal response

The first step to perform TWR post-processing is to decouple the AC component of the measured thermal response of the sample \tilde{T} for calculation of its cross-correlation with the input signal (Equation 1). In preceding studies concerning TWR, this AC component has been obtained by removing the DC component as a low-order polynomial interpolant of the thermal response [6, 21, 22]. Furthermore, due to (i) the latency of the inherent thermal response of the sample to the excitation signal (Figure 8), and (ii) the non-periodicity of the coded waveforms, it is necessary to consider an additional recording time after the end of excitation so that the thermal response to the latest portion of excitation is taken correctly into account. Rather than recording a cooling regime after the excitation, it was shown that extending the end of waveform with an additional step heating is a better approach [22].

In this study, we further consider an additional step heating at the beginning of the waveform. By padding the waveform at *both* sides (0.5 bit on the left, 1 bit on the right, at 50% of max amplitude), a more reliable estimation of the DC component was obtained (see Figure

10(a) for the FPM waveform). Then, the AC component is estimated by removing the DC component as a low order interpolant of the thermal response using the following equation:

$$\tilde{T}(t) = T(t) - \sum_{i=1}^6 a_i t^{p_i}, \quad p = \{0.5 \quad 0.6 \quad 0.7 \quad 0.8 \quad 0.9 \quad 1.0\} \quad (21)$$

where the coefficients a_i are calculated by polynomial fitting of the thermal images in a pixel-wise manner.

Figure 10(b,c) further shows the estimated DC component and AC component of an arbitrary pixel, and demonstrates how the step excitations padded on both sides of the waveform help with proper estimation of the DC component:

- i. The slope of the DC component at the two ends of excitation is reliably determined by avoiding any bias imposed by the phase of relevant sub-pulses, especially when applying FPM waveform with arbitrary phase angle of sub pulses, and
- ii. the delayed thermal response to the last sub-pulse is captured during the 1 bit step excitation at the end of waveform.

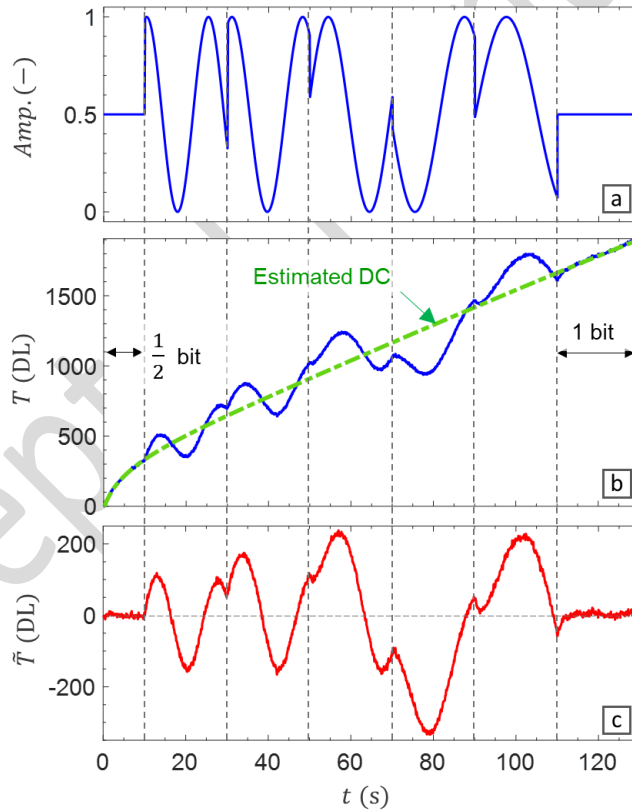


Figure 10: Application of (a) a modified FPM waveform padded on both sides for reliable estimation of (b) the DC component of corresponding thermal response as a low order interpolant and (c) the decoupled AC component, shown for an arbitrary pixel

It is noteworthy that the decoupled AC response to the optical FPM excitation shown in Figure 10(c) is in good agreement with the analytical thermal response to a bipolar FPM waveform as shown in Figure 8(a).

After decoupling the AC component of thermal response, TWR post-processing is performed for the different waveforms and the relevant quantities $peak_{\chi}$, lag_{χ} and φ_{χ} (Equations 2 to 4) are calculated. Then, the lag contrast Δlag_{χ} and phase contrast $\Delta \varphi_{\chi}$ are calculated by subtraction of the corresponding mean value of the selected sound area (see Figure 2(a)).

5.1.2. FPM waveform versus sinusoidal waveforms of different frequencies

In this section the added value of applying a broadband FPM excitation waveform compared to a sinusoidal (i.e. classical lock-in) narrowband excitation of the same duration and amplitude is illustrated. To serve this purpose, the overall depth resolvability of the optimized FPM waveform at the central frequency of 0.05 Hz (i.e. excitation time of 100 s) is compared with three different lock-in excitations of the same duration: (i) a 10-cycle lock-in at 0.1 Hz, (ii) a 5-cycle lock-in at 0.05 Hz (i.e. the same central frequency of FPM waveform), and (iii) a 1-cycle lock-in at 0.01 Hz which is the lowest modulation frequency possible over the excitation time (see Figure 1(a-c)). The comparison is done in terms of phase φ_{χ} which is the standard emissivity-normalized output quantity in case of lock-in thermography. The resulting phase contrast $\Delta \varphi_{\chi}$ maps, together with a cross-section along defect row B are presented in Figure 11.

A relatively high lock-in frequency (Figure 11(a,b)) gives good indication of the more shallow defects, and also provides a good lateral defect sizing due to the fact that the relatively high frequency induces limited lateral heat diffusion. Lowering the lock-in frequency to the lowest frequency of 0.01 Hz clearly reveals its increased sensitivity to deeper defects (Figure 11(c)). But at the same time, it significantly loses phase contrast for more shallow defects. It can be even seen that several shallow defects show an inverted phase contrast, i.e. switching from a negative contrast to a positive contrast (see also Figure 11(e)). This means that the lock-in frequency of 0.01 Hz is close to their so-called blind frequency i.e. the first zero-crossing of the phase spectrum (see [21, 34-36] for more details). Further it should also be noted that using such a low-frequency 1-cycle lock-in excitation (at a frequency much lower than the central frequency of FPM waveform) makes accurate lateral defect sizing more challenging due to the significantly involved in-plane heat diffusion. This will become even worse when inspecting CFRP composites which typically have a dominant in-plane thermal diffusivity [37], or when dealing with longer bit lengths e.g. a 13-bit [23] or a 16-bit [20] Barker code. It should be further noted that reducing the number of lock-in cycles (for a given excitation time) increases the heating duration of each cycle, and therefore, increases the maximum surface temperature. This is an important factor to consider when inspecting composites with thermoplastic matrix in order to avoid possible thermal degradation.

To tackle the aforementioned limitations of narrowband lock-in excitation, broadband excitation waveforms have been considered [6, 15-21]. The broadband 5-bit FPM excitation signal proposed by the current authors [29] was optimized for maximized pulse compression quality in thermographic NDT and maximized overall sensitivity over the depth of the composite. Figure 11(d) shows the phase contrast for the optimized FPM signal in which a high phase contrast is observed over the whole depth of the GFRP sample. Moreover, an increased depth

resolution and lower lateral heat diffusion is observed for FPM as compared to the lowest frequency 1-cycle lock-in (see Figure 11(e) and the slope of phase contrast in the inset). The results clearly confirm the added value of using an optimized broadband excitation signal compared to a narrowband lock-in signal.

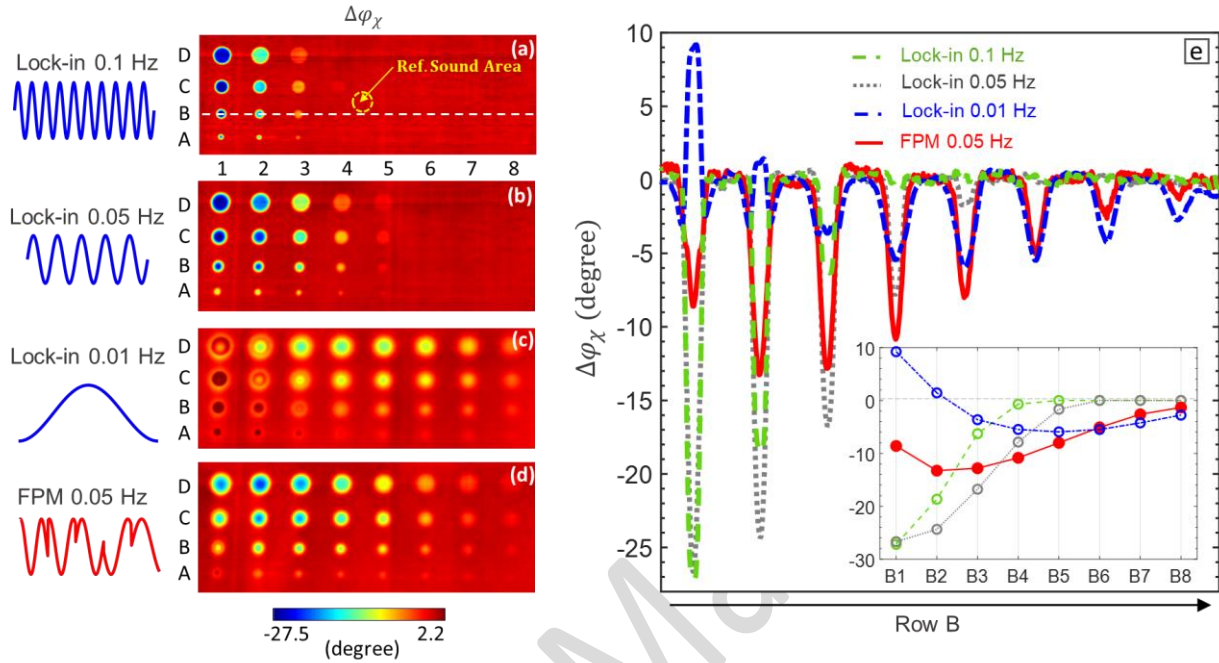


Figure 11: Comparison of the phase maps obtained from excitation waveforms of the same amplitude and the same duration of 100 s for the GFRP sample. (a) 10-cycle lock-in, (b) 5-cycle lock-in, (c) 1-cycle lock-in, (d) FPM waveform, (e) cross-section along row B.

5.1.3. FPM waveform versus conventional waveforms at central frequency 0.05 Hz

After realizing the advantage of a broadband FPM excitation compared to lock-in excitations of the same duration but different frequencies, in this section its performance with respect to sinusoidal and broadband (i.e. frequency sweep and Barker coded) excitation waveforms of the same central frequency is further evaluated in detail.

Figure 12 compares the surface maps of the calculated quantities i.e. (i) normalized $peak_\chi$, (ii) lag contrast Δlag_χ and (iii) phase contrast $\Delta\varphi_\chi$. The four top rows correspond to the classical waveforms and the bottom row corresponds to the optimized FPM waveform. For consistency of the results, the colormap scale of each column is unified so that all its images have the same upper and lower limits.

As the peak of the pulse compressed signal $peak_\chi$ is not an emissivity-normalized quantity, the corresponding surface maps (Figure 12(a-e)) are clearly influenced by the non-uniform heating induced by the two halogen lamps. In order to minimize the effect of non-uniform heating, one may enhance the quality of the peak map by determining and applying the transfer function of the lamps [38, 39]. However, the focus of this study is to evaluate the efficiency of the emissivity-normalized quantities lag_χ and φ_χ (having minimum sensitivity to the non-uniform heating), for which the FPM waveform has been optimized. It is noteworthy that the

physical impact (e.g. the induced in-plane heat diffusion) of the non-uniform heating will anyway affect all quantities, and cannot be compensated by either application of a transfer function or considering emissivity-normalized quantities.

In terms of Δlag_χ (Figure 12(f-j)), lock-in and linear sweep excitation show comparable results, detecting defects up to column 4 which corresponds to a depth of 2 mm, and providing a poor indication of column 5. The lag_χ corresponding to the logarithmic sweep and Barker coded waveform further show a slightly increased contrast and a clear indication of column 5 (2.5 mm deep), while the FPM waveform demonstrates a significantly higher contrast with a minor indication of column 6 (3 mm deep). In terms of phase $\Delta\phi_\chi$ (Figure 12(k-o)), a generally deeper probing depth than Δlag_χ is observed. The phase maps again confirm the enhanced performance of the FPM waveform for all defect sizes, indicating a defect detectability up to the last column 8 (or 4.0 mm deep).

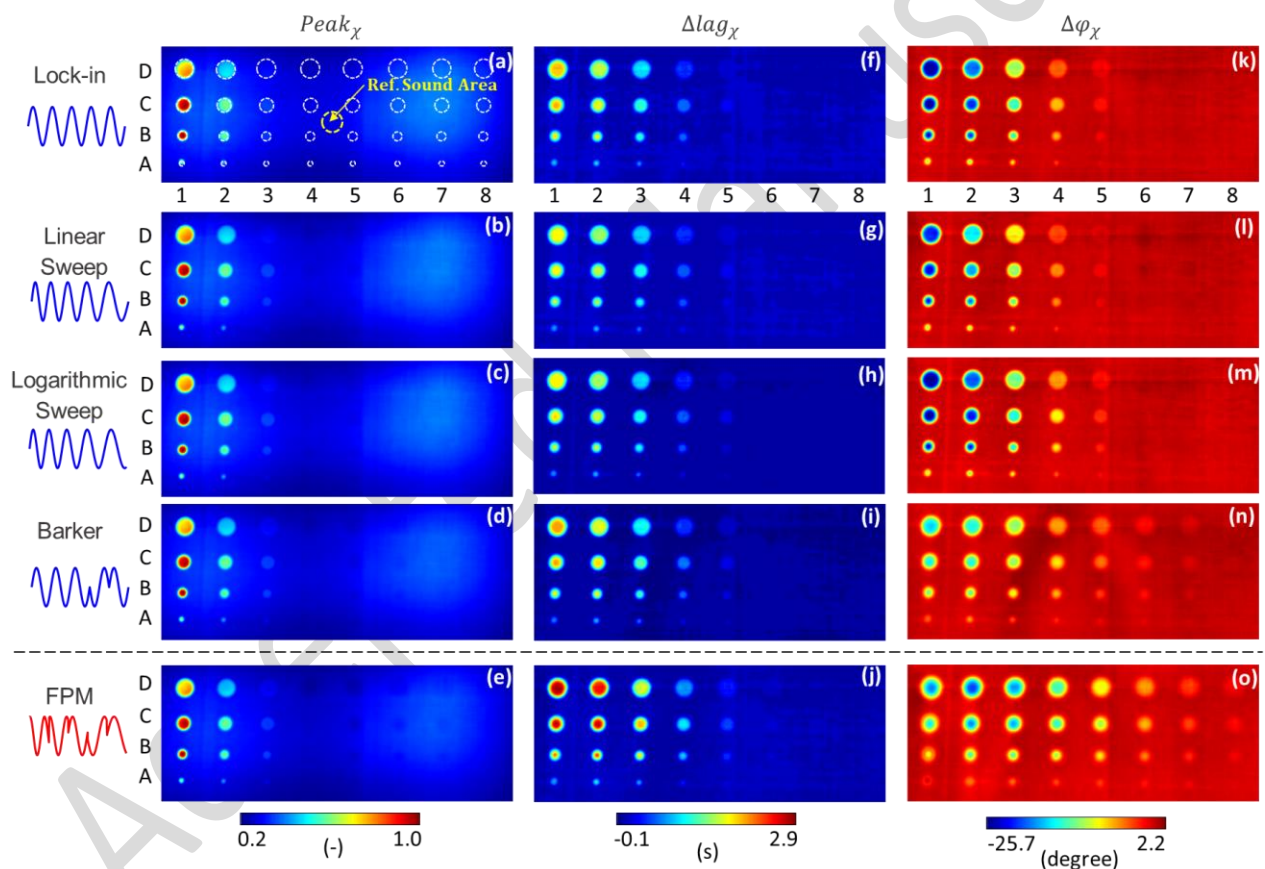


Figure 12: Comparison of full field images of GFRP test coupon with FBHs in terms of (a-e) normalized peak value $peak_\chi$, (f-j) lag contrast Δlag_χ and (k-o) phase contrast $\Delta\phi_\chi$ using the different waveforms at the same central frequency of 0.05 Hz

For a more detailed quantification of the results, the lag contrast Δlag_χ and phase contrast $\Delta\phi_\chi$ along the centerline of (i) row B, (ii) column 5 and (iii) column 7 are shown in Figure 13 and Figure 14. The results of row B are limited to the deeper defects B4 to B8 (the shallow defects

would dominate the vertical range). For clarity, only the algorithmic sweep is included in Figures 13 and 14.

Comparison of the lag and phase contrast, clearly demonstrates that FPM waveform outperforms the other waveforms by far, regardless of the depth and size of the defects. This outperformance is less pronounced for the smallest defects A5 and A7 due to the inherent dominance of lateral heat diffusion compared to the defect's area. Further, the results indicate that the φ_χ has a significantly higher depth resolution and probing depth. The deep column 7 which is entirely transparent to the lag_χ (see Figure 13(c)), is fully resolved by the φ_χ (see Figure 14(c)). Indeed, the lag_χ shows a limited resolution of 0.1 s (corresponding to the sampling frequency of 10 Hz), while the φ_χ has a higher resolution which is not limited by the sampling frequency.

Furthermore, the contrast-to-noise ratio CNR (also indicated as signal-to-noise ratio SNR by some authors [5, 40]) is calculated using the following equation:

$$CNR = \frac{|\bar{\varphi}_{\chi D} - \bar{\varphi}_{\chi S}|}{\sigma_{\varphi S}} \quad (22)$$

where $\bar{\varphi}_{\chi D}$ and $\bar{\varphi}_{\chi S}$ are the average values of the φ_χ over the defected areas and the reference sound area respectively, and $\sigma_{\varphi S}$ is the standard deviation of the φ_χ over the sound area. The CNR values as given in Table 1, indicate that the FPM waveform consistently leads to higher CNR for all considered. Moreover, the defect A8 with the lowest diameter-to-depth ratio ϕ/d of 1.25 is slightly detected by FPM with a CNR of 1.78.

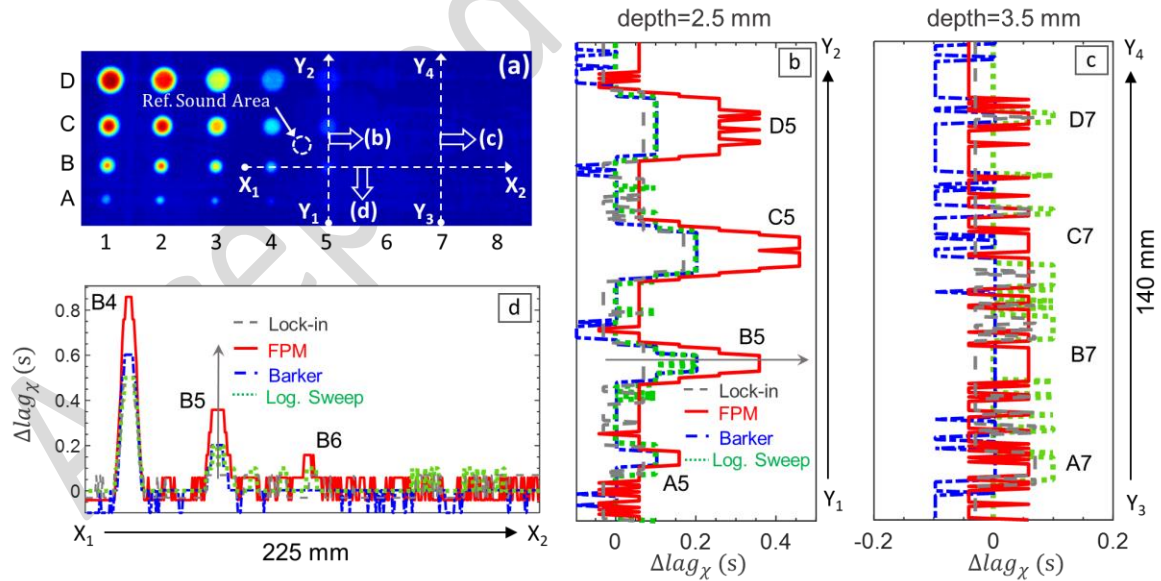


Figure 13: Lag contrast Δlag_χ at central frequency of 0.05 Hz: (a) surface map resulting from FPM waveform, and comparison of the different waveforms along centerline of (b) column 5, (c) column 7 and (d) row B

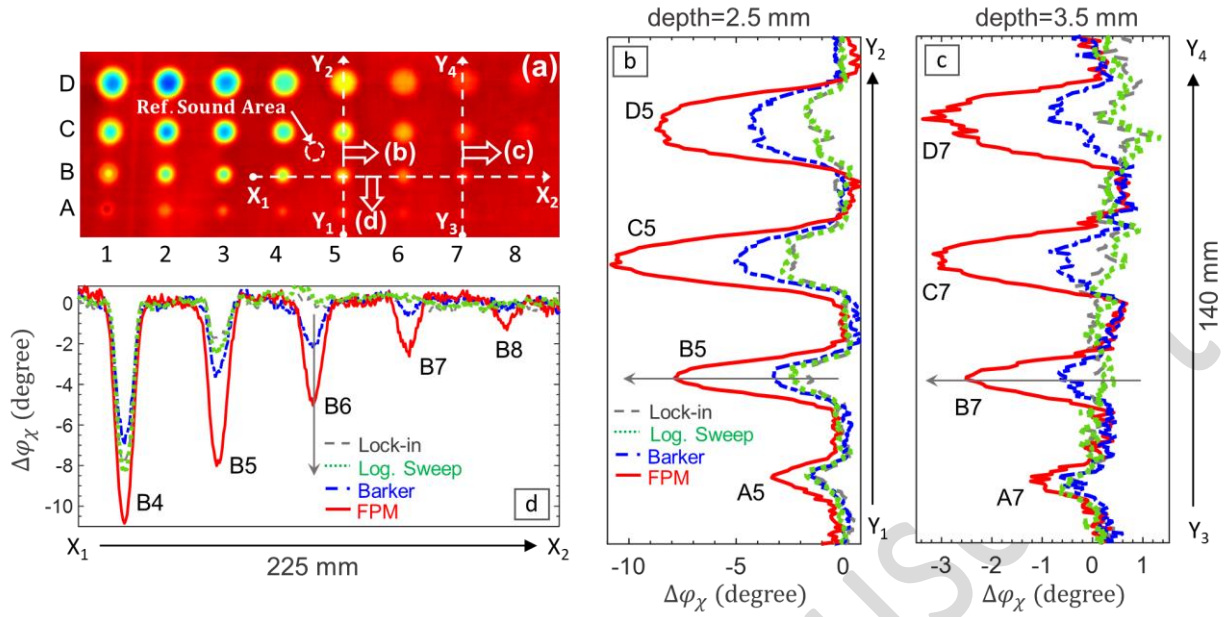


Figure 14: Phase contrast $\Delta\phi_\chi$ at central frequency of 0.05 Hz: (a) surface map resulting from FPM waveform, and comparison of the different waveforms along centerline of (b) column 5, (c) column 7 and (d) row B

Table 1: CNR values of phase ϕ_χ calculated for the defects shown in Figure 14

		Row B					Column 5				Column 7			
		B4	B5	B6	B7	B8	A5	B5	C5	D5	A7	B7	C7	D7
ϕ/d (-)		5.00	4.00	3.33	2.86	2.50	2.00	4.00	6.00	8.00	1.43	2.86	4.27	5.71
CNR(-)	Lock-in	25.16	5.59	0.65	1.36	0.41	2.24	5.60	7.81	4.34	0.59	1.34	1.09	2.62
	Lin. Sweep	19.75	4.28	0.88	1.95	0.42	3.36	4.29	4.60	1.14	0.63	1.94	2.27	3.42
	Log. Sweep	25.53	7.90	0.97	0.96	0.38	4.00	7.89	9.20	4.39	1.35	0.94	1.43	2.47
	Barker	15.45	8.00	5.11	1.03	0.52	2.99	7.98	12.15	10.96	0.81	1.31	1.84	1.35
	FPM	28.08	20.92	13.05	6.39	3.14	4.47	20.87	29.96	25.42	2.77	6.41	9.02	8.30

5.1.4. Evaluation at other central frequencies (0.1 Hz and 0.025 Hz)

In section 5.1 it was shown that application of the optimized FPM waveforms leads to enhanced depth resolvability at the central frequency of 0.05 Hz. The FPM waveform was actually optimized for that central frequency [29]. In this section, the performance of the optimized FPM waveform is evaluated for other central frequencies. For brevity, results are only shown in comparison to the Barker code waveform (which has the best performance among the conventional waveforms).

The obtained results (see Figure 15) clearly demonstrate the effect of the central frequency on the depth resolvability. More importantly, the results indicate that also at other central frequencies, the FPM waveform outperforms the conventional waveforms. In terms of lag_χ , FPM additionally detects the column 4 at 0.1 Hz, and a slight indication of the deepest defects from

column 8 at 0.025 Hz. For the more shallow defects, the FPM waveform leads to a significantly increased contrast of the lag_χ . In terms of the φ_χ , the FPM waveform further detects two additional columns 4 and 5 at 0.1 Hz, and also significantly increases the contrast of defects at 0.025 Hz.

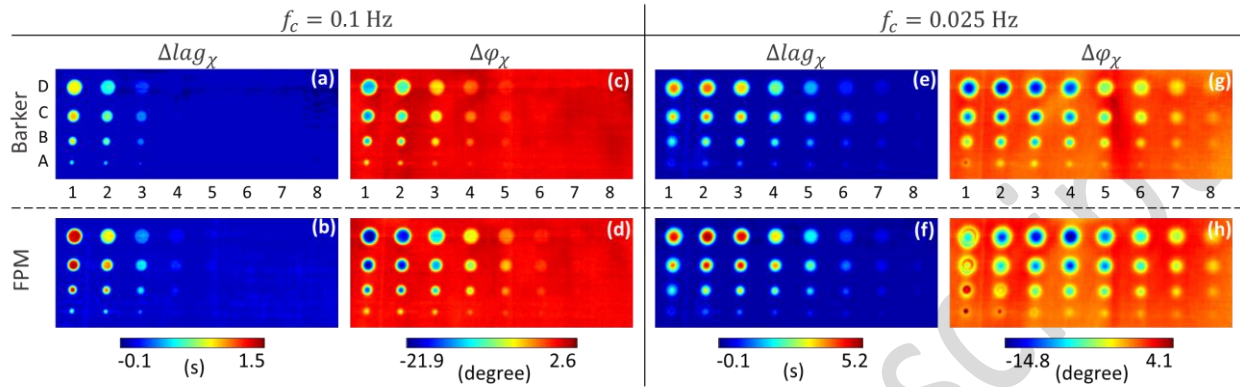


Figure 15: Comparison of full field images of GFRP test coupon with FBHs in terms of (a-b,e-f) lag contrast Δlag_χ and (c-d,g-h) phase contrast $\Delta \varphi_\chi$ of cross-correlation, using different waveforms at different central frequencies (a-d) 0.1 Hz and (e-h) 0.025 Hz

5.2. CFRP sample

Considering that the optimization of the FPM waveform was done through a 1D analytical model, it is of high interest to test its performance for a material which shows a dominant lateral heat diffusion. To this end, a CFRP coupon with flat bottom holes (see section 2) was inspected with the FPM waveform and the conventional waveforms at the central frequency of 0.1 Hz. For brevity, only a comparison between the FPM and Barker coded waveforms is provided. The obtained results are shown in Figure 16. Similar as in previous discussion, the results indicate the outperformance of the FPM waveform particularly in terms of phase φ_χ which provides a clear indication of the deepest defect H3 (see Figure 16(d)). Hence, these results suggest that the framework of optimized FPM waveforms for improved TWR imaging is valid for a wide range of anisotropic media.

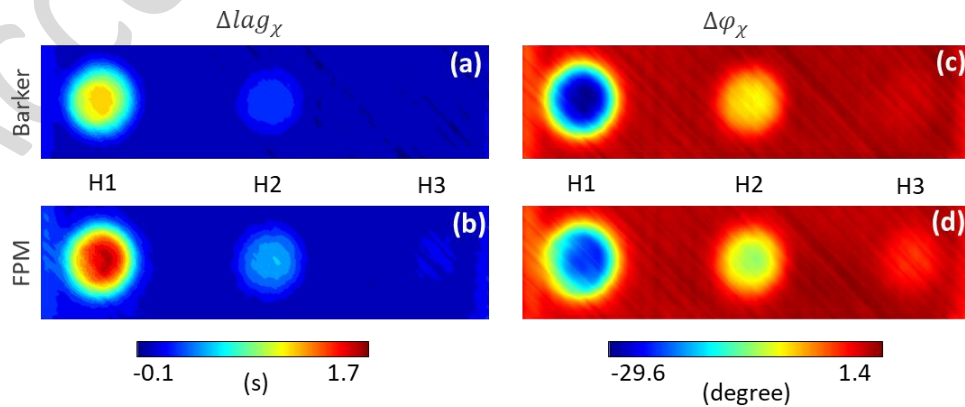


Figure 16: Comparison of full field images of the CFRP test coupon with FBHs in terms of (a-b) lag contrast Δlag_χ and (c-d) phase contrast $\Delta \varphi_\chi$ of cross-correlation, using different waveforms at the central frequency 0.1 Hz

6. Conclusions

A novel frequency-phase modulated (FPM) excitation waveform with optimized modulation code for enhanced depth resolvability of thermal wave radar (TWR) imaging was investigated. Its enhanced depth resolvability (compared to conventional waveforms) was experimentally validated using an optical infrared thermography set-up.

The discretely modulated FPM waveform is comprised of five discontinuous sub-pulses which require fast amplitude modulation (i.e. very short reaction time) of the optical lamps at the modulation points. The response of the halogen lamps to the FPM waveform was measured using a photodiode, and a slight deviation of optical excitation from the input excitation was observed. Moreover, the sensitivity of the depth resolvability of the optimized FPM waveform to the electro-thermal latency of the excitation system was analytically studied in terms of the lag and the phase of TWR. An extreme case with significantly higher latency than the measured one was also simulated. It was shown that even such a high latency is very small compared to the inherent latency of thermal response of the material being inspected, and that it has minor influence on the pulse compression quality and its extracted parameters. Hence, this indicates that a complex FPM excitation waveform does not require any specialized excitation device for inspection of composites, and that standard Halogen lamps suffice.

For the experimental validation of the optimized FPM waveform, a 5 mm thick GFRP test coupon with cross-ply lay-up and multiple defects depths and sizes was tested. The performance of the FPM signal was evaluated compared to sinusoidal (i.e. lock-in), frequency sweep and Barker coded excitation waveforms, all with the same time duration. Different central frequencies (0.025 Hz, 0.05 Hz and 0.1 Hz) were examined and the enhanced defect detection and depth resolvability of the optimized FPM waveforms was confirmed in all cases. Also for a CFRP coupon with highly dominant in-plane heat diffusion, the FPM waveform outperformed the other waveforms in terms of defect detection and depth resolvability.

Acknowledgement

The authors acknowledge the SBO project DETECT-IV (Grant no. 160455), which fits in the SIM research program MacroModelMat (M3) coordinated by Siemens (Siemens Digital Industries Software, Belgium) and funded by SIM (Strategic Initiative Materials in Flanders) and VLAIO (Flemish government agency Flanders Innovation & Entrepreneurship). The authors also acknowledge Fonds voor Wetenschappelijk Onderzoek Vlaanderen (FWO-Vlaanderen) through grants 1S11520N, 1148018N and 12T5418N.

References

1. Yang, R. and Y. He, *Optically and non-optically excited thermography for composites: A review*. Infrared Physics & Technology, 2016. **75**: p. 26-50.
2. Ciampa, F., et al., *Recent advances in active infrared thermography for non-destructive testing of aerospace components*. Sensors, 2018. **18**(2): p. 609.
3. Shepard, S.M., et al. *Enhancement and reconstruction of thermographic NDT data*. in *Proc. SPIE*. 2002.

4. Rajic, N., *Principal component thermography for flaw contrast enhancement and flaw depth characterisation in composite structures*. Composite Structures, 2002. **58**(4): p. 521-528.
5. Madruga, F.J., et al., *Infrared thermography processing based on higher-order statistics*. NDT & E International, 2010. **43**(8): p. 661-666.
6. Gong, J., et al., *Investigation of carbon fiber reinforced polymer (CFRP) sheet with subsurface defects inspection using thermal-wave radar imaging (TWRI) based on the multi-transform technique*. NDT & E International, 2014. **62**: p. 130-136.
7. Yi, Q., et al., *New features for delamination depth evaluation in carbon fiber reinforced plastic materials using eddy current pulse-compression thermography*. NDT & E International, 2019. **102**: p. 264-273.
8. Poelman, G., et al., *Multi-scale gapped smoothing algorithm for robust baseline-free damage detection in optical infrared thermography*. NDT & E International, 2020: p. 102247.
9. He, Z., et al., *Joint Scanning Laser Thermography Defect Detection Method for Carbon Fiber Reinforced Polymer*. IEEE Sensors Journal, 2019. **20**: p. 328 - 336.
10. Poelman, G., et al., *Adaptive spectral band integration in flash thermography: Enhanced defect detectability and quantification in composites*. Composites Part B: Engineering, 2020. **202**: p. 108305.
11. Ibarra-Castaneda, C. and X. Maldague, *Pulsed phase thermography reviewed*. Quantitative Infrared Thermography Journal, 2004. **1**(1): p. 47-70.
12. Badghaish, A.A. and D.C. Fleming, *Non-destructive inspection of composites using step heating thermography*. Journal of composite materials, 2008. **42**(13): p. 1337-1357.
13. Almond, D.P., S.L. Angioni, and S.G. Pickering, *Long pulse excitation thermographic non-destructive evaluation*. NDT & E International, 2017. **87**: p. 7-14.
14. Wu, D. and G. Busse, *Lock-in thermography for nondestructive evaluation of materials*. Revue Générale de Thermique, 1998. **37**(8): p. 693-703.
15. Mandelis, A., *Time-delay-domain and pseudorandom-noise photoacoustic and photothermal wave processes: a review of the state of the art*. IEEE transactions on ultrasonics, ferroelectrics, and frequency control, 1986. **33**(5): p. 590-614.
16. Mandelis, A., *Frequency modulated (FM) time delay-domain thermal wave techniques, instrumentation and detection: a review of the emerging state of the art in QNDE applications*, in *Review of progress in quantitative nondestructive evaluation*. 1987, Springer. p. 799-806.
17. Mulaveesala, R. and S. Tuli, *Implementation of frequency-modulated thermal wave imaging for non-destructive sub-surface defect detection*. Insight-Non-Destructive Testing and Condition Monitoring, 2005. **47**(4): p. 206-208.
18. Mulaveesala, R., J.S. Vaddi, and P. Singh, *Pulse compression approach to infrared nondestructive characterization*. Review of Scientific Instruments, 2008. **79**(9): p. 094901.
19. Tabatabaei, N. and A. Mandelis, *Thermal-wave radar: A novel subsurface imaging modality with extended depth-resolution dynamic range*. Review of Scientific Instruments, 2009. **80**(3): p. 034902.
20. Tabatabaei, N. and A. Mandelis, *Thermal coherence tomography using match filter binary phase coded diffusion waves*. Physical review letters, 2011. **107**(16): p. 165901.
21. Hedayatrasa, S., et al., *Performance of frequency and/or phase modulated excitation waveforms for optical infrared thermography of CFRPs through thermal wave radar: A simulation study*. Composite Structures, 2019. **225**: p. 111177.

22. Silipigni, G., et al., *Optimization of the pulse-compression technique applied to the infrared thermography nondestructive evaluation*. NDT & E International, 2017. **87**: p. 100-110.
23. Shi, Q., et al., *Study on the Detection of CFRP Material with Subsurface Defects Using Barker-Coded Thermal Wave Imaging (BC-TWI) as a Nondestructive Inspection (NDI) Tool*. International Journal of Thermophysics, 2018. **39**(8): p. 92.
24. Shi, Q., et al., *Barker-coded Modulation Laser Thermography for CFRP Laminates Delamination Detection*. Infrared Physics & Technology, 2019. **98**: p. 55-61.
25. Yang, R. and Y. He, *Pulsed inductive thermal wave radar (PI-TWR) using cross correlation matched filtering in eddy current thermography*. Infrared Physics & Technology, 2015. **71**: p. 469-474.
26. Yang, R., et al., *Induction Infrared Thermography and Thermal-Wave-Radar Analysis for Imaging Inspection and Diagnosis of Blade Composites*. IEEE Transactions on Industrial Informatics, 2018. **14**(12): p. 5637-5647.
27. Laureti, S., et al., *Comparative study between linear and non-linear frequency-modulated pulse-compression thermography*. Applied Optics, 2018. **57**(18): p. D32-D39.
28. Tabatabaei, N., *Matched-Filter Thermography*. Applied Sciences, 2018. **8**(4): p. 581.
29. Hedayatrasa, S., et al., *Novel discrete frequency-phase modulated excitation waveform for enhanced depth resolvability of thermal wave radar*. Mechanical Systems and Signal Processing, 2019. **132**: p. 512-522.
30. Wu, S., et al., *Halogen optical referred pulse-compression thermography for defect detection of CFRP*. Infrared Physics & Technology, 2019. **102**: p. 103006.
31. Mahafza, B.R., *Radar Systems Analysis and Design Using MATLAB Third Edition*. 2016: Chapman and Hall/CRC.
32. Horowitz, P. and W. Hill, *The art of electronics*. 1989: Cambridge Univ. Press.
33. Springer, G.S. and S.W. Tsai, *Thermal conductivities of unidirectional materials*. Journal of Composite Materials, 1967. **1**(2): p. 166-173.
34. Bai, W. and B. Wong, *Evaluation of defects in composite plates under convective environments using lock-in thermography*. Measurement science and technology, 2001. **12**(2): p. 142.
35. Quek, S., et al., *A novel and robust thermal wave signal reconstruction technique for defect detection in lock-in thermography*. Measurement Science and Technology, 2005. **16**(5): p. 1223.
36. Pickering, S. and D. Almond. *MATCHED EXCITATION ENERGY COMPARISON OF THE PULSE AND LOCK - IN THERMOGRAPHY NDE TECHNIQUES*. in *AIP Conference Proceedings*. 2009. AIP.
37. Maierhofer, C., et al., *Evaluation of Different Techniques of Active Thermography for Quantification of Artificial Defects in Fiber-Reinforced Composites Using Thermal and Phase Contrast Data Analysis*. International Journal of Thermophysics, 2018. **39**(5): p. 61.
38. Roy, D., K. Chatterjee, and S. Tuli, *Characterization and energy absorption efficiency determination of LED as an effective photothermal excitation source in lock-in thermography*. IEEE Sensors Journal, 2015. **15**(10): p. 6010-6016.
39. Razani, M., A. Parkhimchyk, and N. Tabatabaei, *Lock-in thermography using a cellphone attachment infrared camera*. Aip Advances, 2018. **8**(3): p. 035305.
40. Zalameda, J.N., N. Rajic, and W.P. Winfree. *A comparison of image processing algorithms for thermal nondestructive evaluation*. in *Thermosense XXV*. 2003. International Society for Optics and Photonics.